ring trap. in *Proc. Workshop on Trapped Charged Particles and Fundamental Physics* (eds Dubin, D. & Schneider, D.) *AIP Conf. Proc.* **457,** 269–273 (1999).
12. Schramm, U., Schätz, T. & Habs, D. in *Proc. Conf. on Appl. of Acc. in Research and Industry* (eds Duggan, J. L.) *AIP Conf. Proc.* **576** (in the press).
13. Bryant, P. J. & Johnson, K. *Circular Accelerators and Storage Rings* (Cambridge Univ. Press, Cambridge, 1993).
14. Spreiter, Q., Seurer, M. & Toepffer, C. Relaxation in a strongly coupled particle beam. *Nucl. Instrum. Methods A* **364,** 239–242 (1995).
15. Seurer, M., Spreiter, Q. & Toepffer, C. in *Crystalline Beams and Related Issues* (eds Maletic, D. M. & Ruggiero, A. G.) 311–328 (World Scientific, Singapore, 1996).
16. Raizen, M. G. *et al.* Ionic crystals in a linear Paul trap. *Phys. Rev. A* **45,** 6493–6501 (1992).
17. Drewsen, M., Brodersen, C., Hornekaer, L., Hangst, J. S. & Schiffer, J. P. Large ion crystals in a linear Paul trap. *Phys. Rev. Lett.* **81,** 2878–2881 (1998).
18. Birkl, G., Kassner, S. & Walther, H. Multiple-shell structures of laser-cooled Mg-ions in a quadrupole storage ring. *Nature* **357,** 310–313 (1992).
19. Hasse, R. W. & Schiffer, J. P. The structure of the cylindrically confined Coulomb lattice. *Ann. Phys.* **203,** 419–448 (1990).
20. Habs, D. & Grimm, R. Crystalline ion beams. *Ann. Rev. Nucl. Part. Sci.* **45,** 391–428 (1995).
21. Schiffer, J. P. in *Crystalline Beams and Related Issues* (eds Maletic, D. M. & Ruggiero, A. G.) 217–228 (World Scientific, Singapore, 1996).
22. Wei, J., Okamoto, H. & Sessler, A. M. Necessary conditions for attaining a crystalline beam. *Phys. Rev. Lett.* **80,** 2606–2609 (1998).
23. Blümel, R. *et al.* Phase transitions of stored laser-cooled ions. *Nature* **334,** 309–313 (1988).
24. Dubin, D. H. E. First-order anharmonic correction to the free energy of a Coulomb-crystal in periodic boundary conditions. *Phys. Rev. A* **42,** 4972–4982 (1990).
25. Schiffer, J. P., Drewsen, M., Hangst, J. & Hornekaer, L. Temperature, ordering, and equilibrium with time-dependent forces. *Proc. Natl Acad. Sci. USA* **97,** 10697–10700 (2000).

Acknowledgements

We thank R. Neugart for technical support, and P. Kienle and H. Walther for discussions. The work was partially funded by the Deutsche Forschungsgemeinschaft and the Maier Leibmitz Labor.

Correspondence and requests for material should be addressed to U.S. (e-mail: ulrich.schramm@physik.uni-muenchen.de).

A titanosilicate molecular sieve with adjustable pores for size-selective adsorption of molecules

Steven M. Kuznicki*, Valerie A. Bell*, Sankar Nair†, Hugh W. Hillhouse†, Richard M. Jacubinas*, Carola M. Braunbarth†, Brian H. Toby‡ & Michael Tsapatsis†

** Strategic Technology Group, Engelhard Corporation, 101 Wood Avenue, Iselin, New Jersey 08830, USA*
† Department of Chemical Engineering, 159 Goessmann Laboratory, University of Massachusetts, Amherst, Massachusetts 01003, USA
‡ NIST Center for Neutron Research, National Institute of Standards and Technology, Gaithersburg, Maryland 20899-8562, USA

Zeolites and related crystalline microporous oxides—tetrahedrally coordinated atoms covalently linked into a porous framework—are of interest for applications ranging from catalysis to adsorption and ion-exchange[1]. In some of these materials (such as zeolite rho) adsorbates[2], ion-exchange, and dehydration and cation relocation[3,4] can induce strong framework deformations. Similar framework flexibility has to date not been seen in mixed octahedral/tetrahedral microporous framework materials, a newer and rapidly expanding class of molecular sieves[5–16]. Here we show that the framework of the titanium silicate ETS-4, the first member of this class of materials[8], can be systematically contracted through dehydration at elevated temperatures to 'tune' the effective size of the pores giving access to the interior of the crystal. We show that this so-called 'molecular gate' effect can be used to tailor the adsorption properties of the materials to give size-selective adsorbents[17] suitable for commercially important separations of gas mixtures of molecules with similar size in the 4.0 to 3.0 Å range, such as that of N_2/CH_4, Ar/O_2 and N_2/O_2.

ETS-4 has a mixed octahedral/tetrahedral framework (as shown in the diagram in Fig. 1) with a structure related to the mineral zorite[18–20], and has been described in terms of the random intergrowth of four hypothetical polymorphs[21]. Although larger openings are present in its structure, faulting ensures that access to the crystal interior of ETS-4 occurs through the relatively narrow eight-membered rings (8MRs), analogous to what is seen in small-pore zeolites[22]. The framework structure and cation positions of as-synthesized ETS-4 (Na-ETS-4) and of Sr-exchanged ETS-4 have been recently reported[21,23]. A distinct feature of ETS-4 is the presence of titania semioctahedra that are connected to framework silicon atoms through only four oxygen bridges[18,21], which gives rise to a planar connectivity, in contrast to the three-dimensional connectivity commonly encountered in other microporous frameworks.

As-synthesized ETS-4 has been reported to collapse near 200 °C to an amorphous material owing to the loss of structural water chains present along the channel system[15]. We found that carefully controlled heating leads to a monotonic decrease of the lattice dimensions in all three crystallographic directions, along with the gradual loss of crystallinity. Upon appropriate ion-exchange (for example, with Sr) the thermal stability of the structure, as inferred from diffraction and water adsorption measurements, can be extended to higher temperatures (for example, up to 350 °C for Sr-exchanged ETS-4).

Water-loss curves (as determined by thermal gravimetric analysis, TGA) for as-synthesized and Sr-exchanged ETS-4, along with representative room-temperature powder neutron diffraction patterns of Sr-exchanged ETS-4 after dehydration at temperatures up to 300 °C, are given in Fig. 2a and b, respectively. It is evident that the exchange by Sr leads to higher temperatures for dehydration, and as a result extends the stability range of the ETS-4 framework. The lattice constants, determined from the room-temperature neutron diffraction data, are listed in the Fig. 2 legend, while the evolution of these constants, as determined by *in situ* X-ray diffraction (XRD), is shown in Fig. 2c. A sharp structural transition takes place at ~110 °C, followed by a continuous contraction up to the point when the material becomes amorphous (at temperatures higher than 350 °C). We refer to the dehydrated materials as CTS (contracted titanosilicates). Samples of Sr-exchanged ETS-4 treated at temperatures higher than 250 °C exhibit increasing loss of order, as shown in the powder X-ray and neutron diffraction patterns. Reflections with a k component broaden and disappear first, indicating deformation and eventual breaking of the titania chains that run along the b axis.

The contraction of the CTS samples is preserved on cooling to room temperature in a dry environment. Samples treated at a temperature below 250 °C and rehydrated by exposure to moist air recover their original structure, as determined by XRD. The reversibility of the contraction/expansion phenomenon of ETS-4 points to the well known role of cation relocation on loss of water in inducing framework distortions[24–26]. Samples dehydrated at higher temperatures and exhibiting partial loss of X-ray crystallinity rehydrate more slowly, and do not fully recover their original crystalline structure upon rehydration. The unit cell dimensions of the partially disordered material produced by dehydration of Sr-exchanged ETS-4 at temperatures higher than 330 °C are stable upon exposure to moist air for at least two weeks. The irreversible change to the partially disordered structure (CTS) can be attributed to the destruction of connectivity of the titania chains and consequent loss of the restoring force needed to recover the original structure upon rehydration; strong cation coordination to framework oxygen atoms also promotes this irreversible change. Heat treatment at slightly higher temperatures (>350 °C) leads to complete loss of crystalline order.

Rietveld refinement[27–29] of the powder neutron diffraction data of Fig. 2b revealed a progressive and pronounced effect on the 8MR-opening in dehydrated samples (Fig. 3), in addition to cation

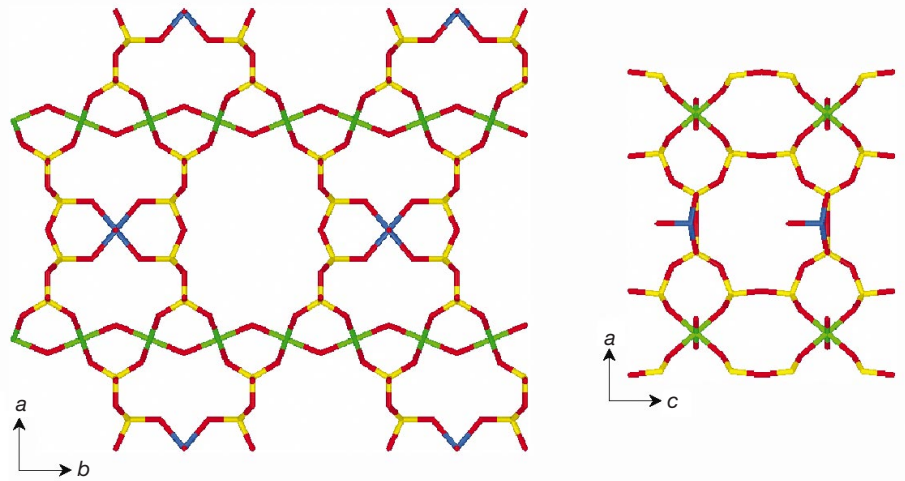

Figure 1 ETS-4 framework. Octahedrally coordinated titanium atoms that form O–Ti–O–Ti–O– chains along the *b* direction are shown in green. The titania semioctahedra of the bridging units that are connected to four framework silicon atoms through oxygen bridges are shown in blue. Silicon and oxygen atoms are shown in yellow and red, respectively. The *a*–*b* slice (left) shows the 12MR opening while the *a*–*c* slice (right) shows the 8MR opening. Pore connectivity along the *a* direction is through 6MRs. As a result, transport of molecules in ETS-4 can be considered to be two-dimensional within the *b*–*c* plane channel system. Owing to faulting, the connectivity of the 12MR down the *c* axis is interrupted and, therefore, transport and access to the interior of ETS-4 is controlled by the 8MR opening.

relocation. More specifically, with the contraction of the unit cell dimensions of ETS-4 during dehydration, the 8MR opening becomes asymmetric, with the D_1 distance (Fig. 3) decreasing monotonically. At the same time, cation relocation takes place and two new cation positions appear. One of the new cation positions (Sr3; see Supplementary Information Table I) is at the centre of the 8MR and its occupancy increases with the temperature of dehydration. Although this new cation position has a low occupancy, it nevertheless has pronounced effects on the access to the crystal interior owing to the two-dimensional connectivity of

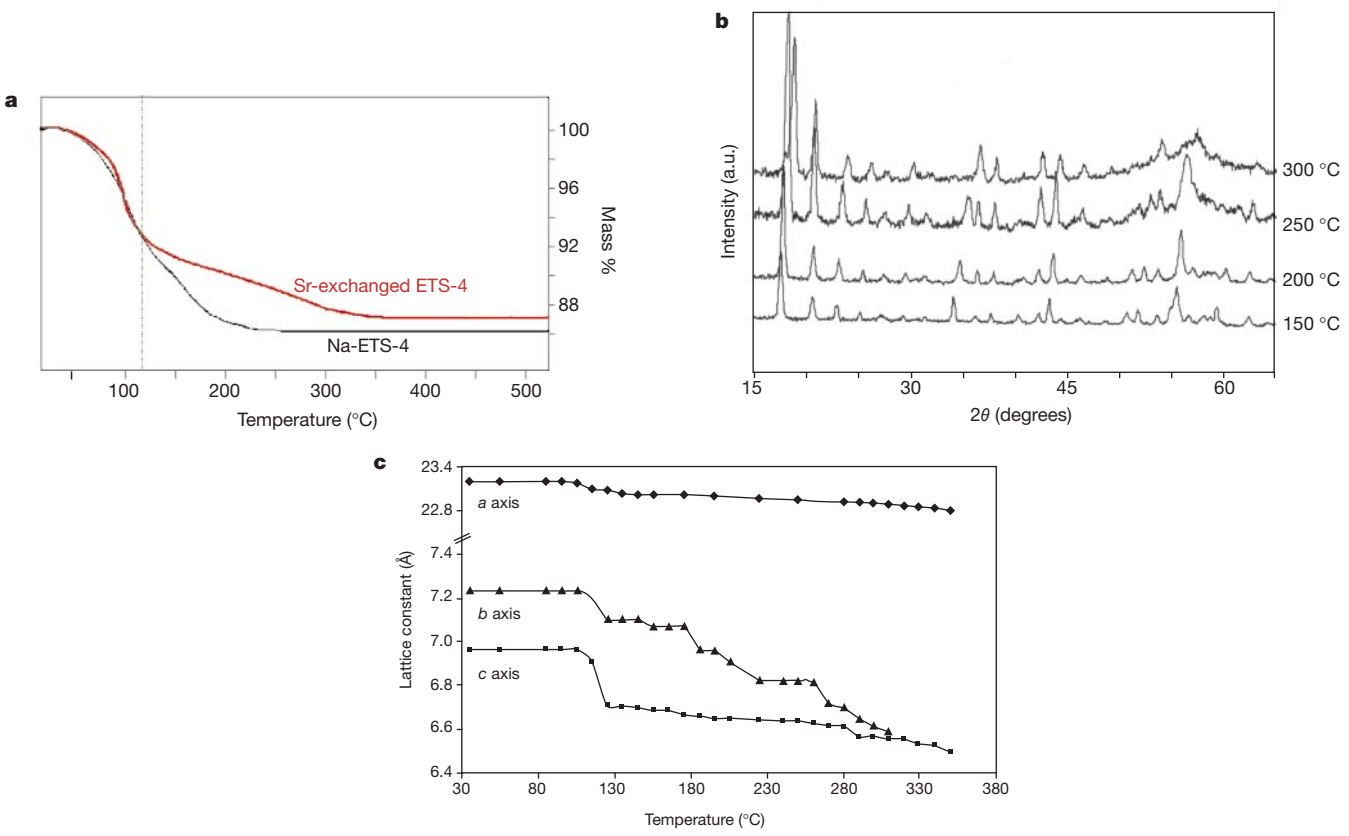

Figure 2 ETS-4 dehydration and associated decrease of the lattice constants. **a**, Thermogravimetric analysis (TGA) showing differences in the water loss of as-synthesized ETS-4 (Na-ETS-4) and Sr-exchanged ETS-4. **b**, Powder neutron diffraction patterns of Sr-exchanged ETS-4 collected at room temperature after dehydration at 150, 200, 250 and 300 °C. The corresponding lattice constants (*a* axis, *b* axis, *c* axis in Å) are: (23.0120, 7.0705, 6.6899), (23.0006, 6.9588, 6.6486), (22.9465, 6.8198, 6.6394), (22.9007, 6.6171, 6.5550) while the Le Bail weighted residuals (R_{wp}) are 1.68, 3.09, 3.41 and 3.56, respectively. The lattice parameters for the as-made sample are 23.1962, 7.2381, 6.965221. **c**, Changes of the lattice constants of Sr-exchanged ETS-4 during heat treatment as determined by *in situ* XRD.

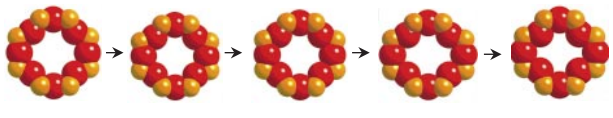

	RT	150°C	200°C	250°C	300°C
D_1(Å)	6.97 (4.27)	6.67 (3.97)	6.65 (3.95)	6.64 (3.94)	6.60 (3.90)
D_2(Å)	7.13 (4.43)	6.72 (4.02)	6.79 (4.09)	7.27 (4.57)	7.27 (4.57)
D_3(Å)	6.31 (3.61)	5.98 (3.28)	5.99 (3.29)	5.97 (3.27)	5.47 (2.77)

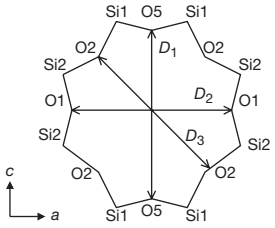

Figure 3 Reduction in the eight-membered ring (8MR) pore opening with increasing dehydration temperature. Oxygen to oxygen distances in the 8MR (D_1, D_2 and D_3) for the room-temperature structure of Sr-exchanged ETS-4 and for the samples dehydrated at 150, 200, 250 and 300 °C were calculated on the basis of atomic positions obtained from Rietveld refinements (see ref. 21, and Supplementary Information Table 1a–d and Fig. 1a–d). Oxygen atoms with identical labels are related by mirror planes. The O5–O5 (D_1) distance is equal to the lattice constant along *c* (see Fig. 2). The numbers in brackets are the effective distances obtained by subtracting twice the oxygen radius (1.35 Å; refs 30, 32) from the distances between the centres of the atoms. For a discussion of the size of the oxygen in molecular sieves, see ref. 32 and references therein. RT, room temperature.

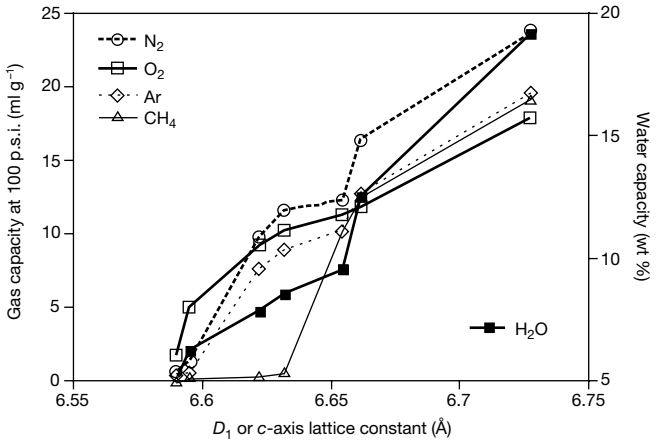

Figure 4 Sorption of molecules of various sizes with lattice contraction of Sr-exchanged ETS-4. This is the material used to provide the data in Figs 2 and 3; adsorption was performed at 25 °C for an equilibration time of 1 hour. 10-hour and 1-hour equilibrations yielded essentially identical results. The dehydration temperatures used to obtain the given D_1 values range from 150 to 350 °C. The corresponding Pauling dimensions[30] are: for CH_4, 4.2 Å; Ar, 3.84 Å; N_2, 4.1 Å (length), 3.00 Å (width); O_2, 3.9 Å (length), 2.8 Å (width); and H_2O, 3.9 Å (length), 3.15 Å (width).

the channel system of ETS-4 (Fig. 1). Both pore narrowing and cation relocation lead to a progressive reduction of the effective diameter of the 8MR.

The progressive contraction of the effective pore size of the 8MR opening profoundly affects the adsorption properties of these materials. Figure 4 shows a clear correlation between a measure of the 8MR opening and the material's adsorption capacity for various gas molecules. We note that although structure refinement of Sr-exchanged ETS-4 dehydrated at temperatures higher than 300 °C was not attempted owing to loss of crystallinity, the D_1 distance (see Fig. 3) of the 8MR opening coincides with the (001) *d*-spacing and can be reliably calculated from X-ray diffraction data. From Figs 2c, 3 and 4 it is evident that as dehydration temperature is increased and effective pore size[30] declines, molecules of progressively smaller dimensions are excluded from adsorption into the crystals.

This phenomenon, the contraction of the unit cell, is cation dependent. It occurs over the temperature regime associated with the loss of those crystal water molecules that are coordinated to the extra-framework cations. Other cation forms than those reported here show similar behaviour (for example, Ba-exchanged ETS-4); however, the specific cation or cation combination has a substantial effect on the temperature range over which shrinkage occurs. Partial exchange with Sr leads to similar behaviour, but the temperature range that leads to framework contraction through dehydration is larger. Figure 5 illustrates size-dependent separation of gas molecules using partially (75%) Sr-exchanged ETS-4 whose 8MR pores have been progressively contracted through dehydration. When the material is calcined at 190 °C, methane is readily adsorbed while the larger ethane molecules are essentially excluded. The capacity for methane absorption declines with further pore contraction; once the material has dehydrated at 270 °C, substantial exclusion occurs whereas the smaller nitrogen molecules are readily absorbed. Dehydration at 300 °C results in sufficiently pronounced pore contraction to show signs of nitrogen exclusion while smaller oxygen molecules can still penetrate the crystal, resulting in an oxygen-selective adsorbent. The dominant cause of loss of gas capacity for a species able to enter the crystal is reduction in crystallinity, with a lesser effect due to lattice shrinkage.

We refer to the ability to systematically manipulate the effective pore size in these materials as the 'molecular gate' effect, which enables the separation of molecules of nearly identical size. An important example is the separation of nitrogen from methane. Nitrogen occurs commonly in natural gas, to the extent that its presence can render many natural-gas reservoirs unusable. As Figs 4 and 5 illustrate, the effective ETS-4 pore size can be manipulated to exclude methane while still allowing the adsorption of the smaller nitrogen molecule. First field demonstrations show that the molecular gate phenomenon allows removal of nitrogen from natural gas (with water vapour contents of 80–150 p.p.m.) at well-head pressures, reducing an initial nitrogen content of 18% to less than 5% with a methane recovery of at least 90%[31]. The system consists of seven pressure-swing adsorption beds with overall process cycling time of 350 seconds, or 50 seconds adsorption per bed. On a laboratory scale, many other separations, including the major constituents of air (Ar/O_2 and N_2/O_2), have been accomplished[17].

The adsorption and structural results point to the contraction of the 8MRs and concomitant cation relocation as being primarily responsible for the gradual exclusion of smaller and smaller molecules. However, some contributions may be due to the presence and potential pore-blocking role of extra-framework species, which may result from the progressive loss of crystalline order that accompanies pore contraction. We have industrially manufactured ETS-4 on a multi-ton scale, using standard equipment and raw materials common to the zeolite industry. Despite the unit-cell contraction and disorder induced by dehydration, it retains adsorption capacities and uptake rates suitable for practical applications. For example, the adsorption step in removing nitrogen from natural gas can be completed in less than one minute. The kinetic stability of ETS-4 to rehydration allows the material to be used in relatively humid process streams. We have a pilot plant that has successfully purified methane using raw, wet natural gas for nearly two years. These features, and the ability to tune the effective pore size of ETS-4, make it an attractive system for a range of important and difficult gas separation applications. □

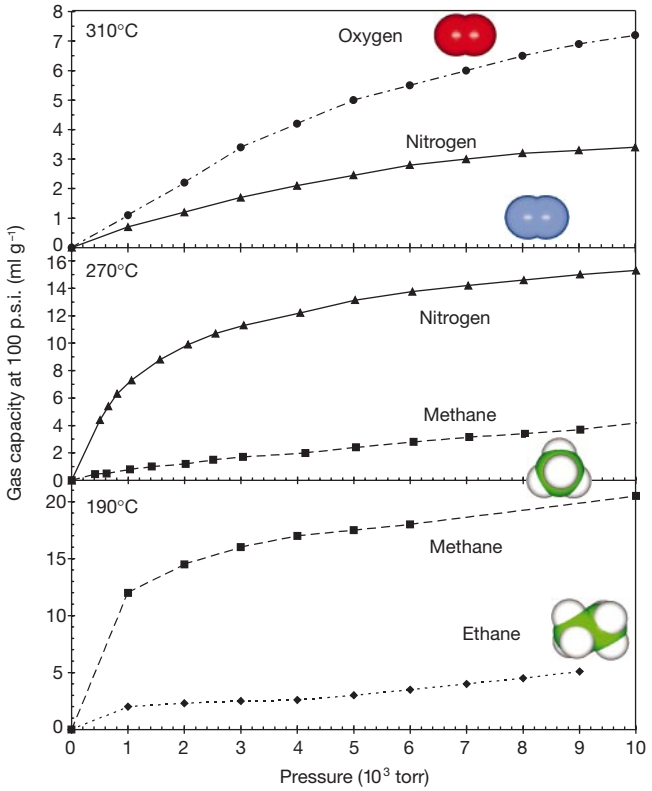

Figure 5 The molecular gate effect. Adsorption isotherms (collected at room temperature) for NaSr-ETS-4 (partially (75%) Sr-exchanged ETS-4) dehydrated at 190, 270 and 310 °C demonstrate that the corresponding CTS materials show selectivity for methane over ethane, nitrogen over methane and oxygen over nitrogen, respectively. The molecule shape illustrations were constructed using Mopac, as implemented in the Insight II (v4.0.0) software suite (Molecular Simulations Inc., San Diego, California, 1996).

Methods

Synthesis and characterization

ETS-4 synthesis and ion exchange were performed as described elsewhere[17,21]. *In situ* X-ray diffraction was performed using a Philips X'Pert diffractometer equipped with a high-temperature stage employing a Si internal standard. TGA was performed in a DSC/TGA (differential scanning calorimetry/thermogravimetric analysis) system with a heating rate of 0.5 °C min^{-1} in air and a flow rate of 10 litres per hour. ICP-MS (inductively coupled plasma-mass spectrometry) was used to determine the degree of ion-exchange. Adsorption data (Fig. 4) were collected in a VTI HPA-300 at 100 p.s.i. and 30 °C after dehydration for 24 h at the required temperature. Adsorption isotherms (Fig. 5) were collected, by VTI Corp., in a VTI HPA-300 at 25 °C, after 24 h of dehydration at the required temperature.

For the neutron diffraction studies, samples of Sr-exchanged ETS-4 were heat-treated at the required temperature for 24 h in Pyrex vials under dry helium flow. The vials were then sealed, isolated from the helium stream, and stored in a dry helium atmosphere. The samples were subsequently transferred to indium-sealed vanadium sample holders under a dry helium atmosphere. Neutron diffraction patterns were collected between 2θ values of 6° and 130° on the high-resolution BT-1 powder diffractometer at NIST (Gaithersburg, MD), operating at a wavelength of 2.0783 Å with a Ge(311) monochromator and a 15′ Soller collimator for high neutron flux.

Structure analysis

The room-temperature structure of Sr-ETS-4 in the *Cmmm* space group (solved from X-ray data) was taken as a starting point for the solution of the contracted structure. Analysis of neutron diffraction data from the material heat treated at 150, 200, 250 and 300 °C shows that *Cmmm* symmetry is retained to a good approximation. First, structure factors were extracted from the neutron diffraction data using the Le Bail algorithm[27]. The lattice constants (in the *Cmmm* space group), diffractometer zero, scale factor, background, and profile parameters were refined using this extraction technique before any atomic parameters were varied. The lattice constants and weighted residuals using the Le Bail fit are given in the legend of Fig. 2 and represent the best possible fit using the *Cmmm* space group.

A detailed structural analysis was performed on the samples dehydrated at 150, 200, 250 and 300 °C. Fourier difference maps were used to locate the Sr^{2+} cations in the framework for these cases. Three cation positions are located and refined in these structures. Three-site occupancy constraints are used to satisfy both the overall charge balance as well as the total number of cations as known from the room-temperature structure. Two of the cation sites have relatively low occupancies. One of them is the original Sr^{2+} cation site in the room-temperature structure, and the other is a new site located at the centre of the 8MR, in which case the cation coordinates to the oxygen atoms of the 8MR. The third site is heavily occupied, and is also a new cation position. There is another significant peak observed in the Fourier maps which, owing to its coordination environment, is attributed to residual water still adsorbed in the framework. The oxygen (Ow) occupancy on this site decreases significantly with increasing dehydration temperature, in agreement with thermogravimetric data.

Structure refinement

After identifying these structural changes, we conducted Rietveld refinement[28,29] of the data for the samples dehydrated at 150, 200, 250 and 300 °C. However, owing to the low number of observed diffraction peaks and disorder in the material, soft constraints were necessary throughout the refinement—elimination of these constraints results in divergences in the model. The weight of the bond-angle constraints was set to 10% of the weight of the bond-distance constraints, and results in physically realistic bond distances and bond angles. Tables 1a, 1b, 1c and 1d in the Supplementary Information show the refined cation and framework structural parameters. The lattice constants obtained from the Le Bail fit are further refined, with only minor changes occurring in their values. Figures 1a, 1b, 1c and 1d in Supplementary Information show the fitted neutron diffraction patterns for the cases considered here. The fits are reasonably good, and are close to the best possible values in the *Cmmm* space group, as obtained by the Le Bail profile fit.

Received 24 November 2000; accepted 21 June 2001.

1. Hammonds, K. D., Heine, V. & Dove, M. T. Rigid-unit modes and the quantitative determination of the flexibility possessed by zeolite frameworks. *J. Phys. Chem. B* **102,** 1759–1767 (1998).
2. Mentzen, B. F. & Gelin, P. The silicalite p-xylene system. 1. Flexibility of the MFI framework and sorption mechanism observed during p-xylene pore-filling by X-ray powder diffraction at room temperature. *Mater. Res. Bull.* **30,** 373–380 (1995).
3. Nenoff, T. M. *et al.* Flexibility of the zeolite RHO framework. In situ X-ray and neutron powder structural characterization of cation exchanged BePO and BeAsO RHO analogs. *J. Phys. Chem.* **102,** 14256–14264 (1996).
4. Johnson, G. M. *et al.* Flexibility and cation distribution upon lithium exchange of aluminosilicate and aluminogermanate materials with RHO topologies. *Chem. Mater.* **11,** 2780–2787 (1999).
5. Kuznicki, S. M. Large-pored crystalline titanium molecular sieve zeolites. US Patent No. 4853202 (1989).
6. Kuznicki, S. M. & Thrush, K. A. Large-pored molecular sieves with charged octahedral titanium and charged tetrahedral aluminum sites. US Patent No. 5244650 (1993).
7. Kuznicki, S. M. & Thrush, K. A. Large-pored molecular sieves containing at least one octahedral site comprising titanium and at least silicon as a tetrahedral site. US Patent No. 5208006 (1993).
8. Kuznicki, S. M. Preparation of small-pored crystalline titanium molecular sieve zeolites. US Patent No. 4938939 (1990).
9. Anderson, M. W. *et al.* Structure of the microporous titanosilicate ETS-10. *Nature* **367,** 347–351 (1994).
10. Anderson, M. W. *et al.* Microporous titanosilicate ETS-10, a structural survey. *Phil. Mag. B* **71,** 813–841 (1995).
11. Wang, X. & Jacobson, A. J. Crystal structure of the microporous titanosilicate ETS-10 refined from single crystal X-ray diffraction data. *Chem. Commun.* 973–974 (1999).
12. Anderson, M. W. *et al.* Isomorphous substitution in the microporous titanosilicate ETS-10. *Microporous Mater.* **6,** 195–204 (1996).
13. Eldewik, A., Luca, V., Singh, N. K. & Howe, R. F. Iron substitution in the microporous titanosilicate ETS-10. *Proc. Int. Zeolite Conf.* **3,** 1507–1514 (1998).
14. Lamberti, C. Electron-hole reduced effective mass in monoatomic –OTiOTiO– quantum wires embedded in the siliceous crystalline matrix of ETS-10. *Microporous Mesoporous Mater.* **30,** 155–163 (1999).
15. Rocha, J. & Anderson, M. W. Microporous titanosilicates and other novel mixed octahedral-tetrahedral framework oxides. *Eur. J. Inorg. Chem.* 801–818 (2000).
16. Bordiga, S. *et al.* Stoichiometric and sodium-doped titanium silicate molecular sieve containing atomically defined -OTiOTiO- chains: Quantum ab initio calculations, spectroscopic properties, and reactivity. *J. Chem. Phys.* **112,** 3859–3867 (2000).
17. Kuznicki, S. M., Bell, V. A., Petrovic, I. & Desai, B. T. Small-pored crystalline titanium molecular sieve zeolites and their use in gas separation processes. US Patent No. 6068682 (2000).
18. Sandomirskii, P. A. & Belov, N. V. The OD structure of zorite. *Sov. Phys. Crystallogr.* **24,** 686–693 (1979).
19. Mer'kov, A. N. *et al.* Raite and zorite, new minerals from the Lovozero tundra. *Zap. Vses. Mineral. Obshchest.* **102,** 54–62 (1973).
20. Philippou, A. & Anderson, M. W. Structural investigation of ETS-4. *Zeolites* **16,** 98–107 (1996).
21. Braunbarth, C. *et al.* Structure of strontium ion exchanged ETS-4 microporous molecular sieves. *Chem. Mater.* **12,** 1857–1865 (2000).
22. McCusker, L. B. in *Comprehensive Supramolecular Chemistry, Solid-State Supramolecular Chemistry: Two- and Three- Dimensional Inorganic Networks* (eds Alberti, G. & Bein, T.) 393–423 (Pergamon, New York, 1996).
23. Cruciani, G., De Luca, P., Nastro, A. & Pattison, P. Rietveld refinement of the zorite structure of ETS-4 molecular sieves. *Microporous Mesoporous Mater.* **21,** 143–153 (1998).
24. Bieniok, A. & Hammonds, K. D. Rigid unit modes and the phase transition and structural distortions of zeolite rho. *Microporous Mesoporous Mater.* **25,** 193–200 (1998).
25. Bieniok, A. & Baur, W. H. A large volume contraction accompanies the low- to high- temperature transition of zeolite Sr-RHO. *J. Solid State Chem.* **90,** 173–182 (1991).
26. Depmeier, W. in *Molecular Sieves* Vol. 2, *Structures and Structure Determination* (eds Karge, H. J. & Weitkamp, J.) 113–140 (Springer, Berlin, 1999).
27. Le Bail, A., Duroy, H. & Fourquet, J. L. Ab-initio structure determination of $LiSbWO_6$ by X-ray powder diffraction. *Mater. Res. Bull.* **23,** 447–452 (1988).

28. Young, R. A. (ed.) *The Rietveld Method* (Oxford Univ. Press, Oxford, 1993).
29. Larson, A. C. & von Dreele, R. B. *GSAS Report LAUR 86-784* (Los Alamos National Laboratory, 1986).
30. Breck, D. W. *Zeolite Molecular Sieves* (Wiley, New York, 1974).
31. Mitariten, M. & Dolan, W. Nitrogen removal from natural gas with molecular gate technology. *Proc. Laurance Reid Gas Cond. Conf.* **51,** 1–16 (2001).
32. Abrams, L. & Corbin, D. R. in *Topics in Inclusion Science* Vol. 6, *Inclusion Chemistry with Zeolites: Nanoscale Materials by Design* (eds Herron, N. & Corbin, D. R.) 4–6 (Kluwer, Dordrecht, 1995).

Supplementary information is available on *Nature*'s World-Wide Web site (http://www.nature.com) or as paper copy from the London editorial office of *Nature*.

Acknowledgements

We thank J. Curran for discussions and assistance in the preparation of the manuscript, and VTI Corp. for the data of Fig. 5. This work was supported by ATP/NIST, the David and Lucile Packard Foundation and NSF-CTS.

Correspondence and requests for materials should be addressed to S.M.K. (e-mail: steve.kuznicki@engelhard.com).

The timing of the last deglaciation in North Atlantic climate records

Claire Waelbroeck*, Jean-Claude Duplessy*, Elisabeth Michel*, Laurent Labeyrie*†, Didier Paillard* & Josette Duprat‡

** Laboratoire des Sciences du Climat et de l'Environnement, Domaine du CNRS, bât. 12, 91198 Gif-sur-Yvette, France*
† Département des Sciences de la Terre, Université Paris-sud Orsay, bât. 504, 91104 Orsay, France
‡ Département de Géologie et Océanographie, CNRS UMR 5805, Université de Bordeaux I, Talence, France

To determine the mechanisms governing the last deglaciation and the sequence of events that lead to deglaciation, it is important to obtain a temporal framework that applies to both continental and marine climate records. Radiocarbon dating has been widely used to derive calendar dates for marine sediments, but it rests on the assumption that the 'apparent age' of surface water (the age of surface water relative to the atmosphere) has remained constant over time[1,2]. Here we present new evidence for variation in the apparent age of surface water (or reservoir age) in the North Atlantic ocean north of 40° N over the past 20,000 years. In two cores we found apparent surface-water ages to be larger than those of today by 1,230 ± 600 and 1,940 ± 750 years at the end of the Heinrich 1 surge event (15,000 years BP) and by 820 ± 430 to 1,010 ± 340 years at the end of the Younger Dryas cold episode. During the warm Bølling–Allerød period, between these two periods of large reservoir ages, apparent surface-water ages were comparable to present values. Our results allow us to reconcile the chronologies from ice cores and the North Atlantic marine records over the entire deglaciation period. Moreover, the data imply that marine carbon dates from the North Atlantic north of 40° N will need to be corrected for these highly variable effects.

The last deglaciation is a period particularly well dated because it belongs to the time span covered by isotopic (^{14}C) dating techniques, which can be applied to both continental and marine sediments. Moreover, ^{14}C dates can be converted into calendar ages through calibration curves describing the variations in the atmospheric $^{14}C/^{12}C$ ratio over the past 20 kyr (ref. 3). Also, the uncertainty on the absolute dating by annual-layer counting of the Greenland ice cores is small (<550 yr) over the last 15 kyr (ref. 4). Therefore, it is possible to compare directly the timing of events from continental and ice-core records, and thus to infer causal mechanisms from the data. The situation is more complex for the marine data, as the ^{14}C dates are measured on foraminifera preserved in the sediments and hence reflect the $^{14}C/^{12}C$ ratio of the water in which the foraminifera calcified. The surface-water $^{14}C/^{12}C$ ratio is different from that of the contemporaneous atmosphere, reflecting the balance between the input of atmospheric ^{14}C and its removal by transport and radiodecay in the water column. This difference in $^{14}C/^{12}C$ ratio is usually expressed as the apparent or reservoir age of the water mass.

A compilation of pre-bomb surface-water ^{14}C content indicates that the modern surface reservoir age is about 400 ± 100 yr in the tropics and in the North Atlantic whereas it rises to 1,200 yr at higher latitudes in the Southern and North Pacific oceans[5,6]. Past reservoir ages most probably differed from those of today, but only sparse data exist. Reservoir ages have been measured in a few sites at given times in the past, by dating contemporaneous samples in marine sediments and in terrestrial organic matter, marked by the same volcanic ash layer[7–10].

Here, we present summer sea surface temperature (SST) reconstructions and benthic oxygen isotopic records ($\delta^{18}O_b$) from three sediment cores raised for the North Atlantic Ocean between 37 and 55° N (SU 81-18, 37° 46′ N, 10° 11′ W, 3,135 m; CH 69-09, 41° 45′ N, 47° 21′ W, 4,100 m; and NA 87-22, 55° 29′ N, 14° 41′ W, 2,161 m). These records have been dated by accelerator mass spectrometry on monospecific planktonic foraminifera samples[1,11,12] (see Supplementary Information Table 1). Radiocarbon ages have been converted into calendar ages with the CALIB 4.1 software[13], the smoothed (310-yr moving average) 1998 marine calibration curve

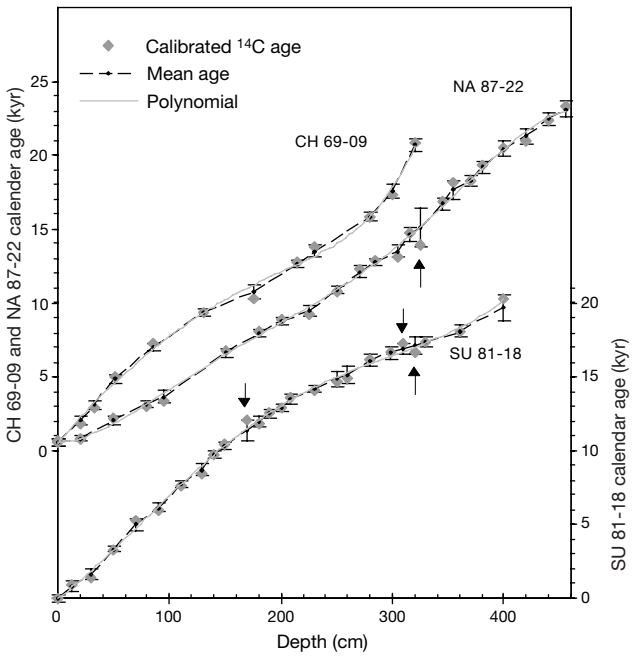

Figure 1 Age–depth relationships for the three North Atlantic deep sea cores. Calendar ages were calculated from the measured ^{14}C ages (see Supplementary Information Table 1) with the CALIB 4.1 software[13] and a constant surface reservoir age of 400 yr. For each core, two different interpolation schemes were used: first, we computed the fifth-order polynomial fitting the dated levels (grey line); second, we linearly interpolated the dated levels, leaving out one age in core NA 87-22 and three ages in core SU 81-18 that showed small age inversions (arrows). The error on the linearly interpolated age scale is taken as one standard deviation of the sample's calendar-age probability distribution given by CALIB 4.1. The error on the polynomial age scale is taken as the difference between the actual sample calendar age and the polynomial age computed at the same level, when this difference is larger than the error on the sample's calendar age. It is otherwise equal to the error on the linearly interpolated age scale. We derived the final age model for each core (black dots with 1-s.d. error bars) by taking the arithmetical mean of the above two timescales to ensure realistically large error bars. The final error estimate includes an additional 200-yr uncertainty, representing the maximum possible bioturbation bias. Both interpolation schemes support our conclusions.